Journal of Computational and Applied Mathematics 391 (2021) 113454

Contents lists available at ScienceDirect

Journal of Computational and Applied Mathematics

journal homepage: www.elsevier.com/locate/cam

Numerical simulation of a thermal Ice Protection System including state-of-the-art liquid film model

Bárbara Arizmendi Gutiérrez, Alberto Della Noce, Mariachiara Gallia, Tommaso Bellosta, Alberto Guardone *

Department of Aerospace Science and Technology, Politecnico di Milano, Via La Masa 34, 20156 Milano, Italy

ARTICLE INFO

Article history:
Received 29 September 2020
Received in revised form 22 December 2020

Keywords:
In-Flight Icing
Liquid films
Ice Protection Systems
Heat exchange

ABSTRACT

In this work, a numerical model for the operation of an electro-thermal Ice Protection Systems (IPS) for an airfoil is presented. The present model solves the energy conservation laws and includes a boundary layer model to compute the relevant aerodynamic quantities based on previous works. Additionally, the computation of aerodynamic and water impingement properties is performed by means of open-source and in-house developed software. A state-of-the-art liquid film model based on lubrication theory has been deployed as an alternative to an element-wise mass balance. A simple ice formulation for the prediction of the formation of runback ice has been included. Moreover, a robust evaporation model based on the heat and mass transfer analogy is deployed. Finally, an interpolation scheme for the element-wise enthalpy variation is presented. The results obtained are in good agreement with the experimental data from the open literature for a range of different test cases including different operating modes, environmental and flight conditions.

1. Introduction

Since the very early years of flight, a crucial design problem has been to protect aircraft from the adverse effects of ice accretion. Icing occurs when an air-vehicle flies through wet air and water droplets' temperature is below freezing at the impact with surface [1]. These particles can freeze and form ice on wing leading edges, engine intakes, Pitot probes, propellers and vents. Ice formations lead to performance degradation since they modify the aerodynamic shape reducing lift, increasing drag and causing a reduction of control and stability [2]. Moreover, ice can cause engine and measurement tools failure [3] or under-performance.

To guarantee safe flight in icing conditions, aircraft are equipped with Ice Protection Systems (IPS) to avoid, to delay or to remove ice accretion. The two main operation modes of IPS are the de-icing and the anti-icing. In the former operation, ice formations are removed once the system is actuated while in the latter the system prevents ice accretion on the surface by continuously operating. Furthermore, thermal anti-icing systems can operate in two regimes [4]: fully evaporative, when all the water that impacts is evaporated or the runback water area remains inside the protected zone and running wet, when runback water flows past the IPS. This condition might cause water to freeze in unprotected regions forming the so-called runback ice.

* Corresponding author.
E-mail address: alberto.guardone@polimi.it (A. Guardone).

https://doi.org/10.1016/j.cam.2021.113454
0377-0427/

Nomenclature

Greek letters

β	Collection Efficiency
δ	Thickness [m]
μ	Dynamic viscosity [Pa/s]
ρ	Density [kg/m^3]
τ	Shear stress [Pa]
ε	Numerical tolerance
φ	Angle of impingement

Parameters

$\dot{m}$	Mass flow rate [kg/s]
$\dot{m}''$	Mass flux [kg/(m^2 s)]
$\dot{Q}$	Heat flow rate [W]
$\mathcal{R}$	Universal gas constant [J/(mol K)]
$\mathfrak{M}$	Molar mass [mol]
Le	Lewis number
Nu	Nusselt number
Pr	Prandtl number
Sc	Schmidt number
Sh	Sherwood number
St	Stanton number
A	Control volume area [m^2]
A'	Layer control volume cross section area [m^2]
B_m	Mass transfer driving force
C_f	Skin friction coefficient
C_P	Pressure coefficient
c_p	Specific heat at constant pressure [J/(kg K)]
F	Wetness factor
g_m	Mass conductance [kg/(m^2 s)]
H	Airfoil skin thickness [m]
h	Heat transfer coefficient [W/(m^2 K)]
i	Latent heat [J/kg]
k	Thermal conductivity [W/(m K)]
M	Water vapor mass fraction in air
p	Pressure [Pa]
r	Recovery factor
s	Curvilinear abscissa [m]
T	Temperature [K]
t	Thickness of a substratum layer [m]
U	Global heat transfer coefficient [W/(m^2 K)]
u	Velocity [m/s]
V	Droplet velocity [m/s]

Subscripts

0	Stagnation point
∞	Freestream
air	Air flow
$cond$	Conduction
e	External edge of boundary layer
$evap$	Evaporative
f	Liquid film

G	Region of moist air on the freestream flow
H_2O	Water
ice	Ice
imp	Impinging
in	Finite volume inflow
IPS	Ice protection system
$l-s$	Solidification of water
$l-v$	Vaporization of water
out	Finite volume outflow
rec	Recovery
ref	Reference for computing the sensible enthalpy
S	Region of saturated vapor just above the liquid film
s	Curvilinear abscissa
sat	Saturation
wall	Airfoil solid surface

A widely used technology is the electro-thermal protection and it is the preferred method for rotor blades and probes due to its reduced weight, adaptability to complex surfaces and flexibility to operate in different regimes. The electro-thermal protection heats surfaces at risk of ice accretion exploiting the Joule effect occurring when an electric current goes through a resistive component. The main drawback of this technology is that requires a large energy consumption to operate in evaporative regimes on large surfaces, such as wings.

The physical problems related to in-flight icing are complex and multidisciplinary. Several feasibility restrictions limit their experimental investigation such as their cost and the availability of suitable facilities. Therefore, it is an application that requires the development of sophisticated and representative numerical models, among others, for the phase change problem, for the liquid film and for aerodynamics [5–7]. To what concerns anti-ice IPS, very limited experimental measurements are publicly available in the open literature. Regarding the experimental study of wing electro-thermal IPS, Al-Khalil et al. performed a set of icing wind tunnel tests of an electro-thermal IPS in different environmental conditions [4].

As a consequence, there is a large research effort on the development of numerical models for the prediction of the performance of an electro-thermal anti-ice IPS. These aim to support the preliminary design of these systems and to improve the understanding of the physics of the phenomenon. An accurate understanding and simulation of the physics could help their design and optimization processes. Moreover, it could help identify critical conditions and reduce the number and duration of expensive test campaigns.

A research effort has been conducted on the numerical modeling of anti-ice systems. For this operating regime, studies mainly focus on the evaluation of the surface temperature and of the runback water mass flux. The evaluation of these quantities requires an accurate computation of the heat transfer coefficients of air and water. The study of runback water is needed to determine the amount of water that is evaporated, to evaluate how the liquid portion flows over the surface and the possible formation of runback ice. In addition, the evaluation of the surface temperature is necessary to determine the heat fluxes and it can be useful to study materials degradation.

The numerical models reported in the literature are based on the solution of the mass and energy conservation laws in a discrete computational domain. Moreover, a boundary layer model is deployed to compute the required aerodynamic properties. One numerical model proposed is ANTICE [8,9]. This model solved two differential energy conservation laws for the multilayered solid surface and the liquid film. The equations were numerically solved by means of a finite volume scheme. The boundary layer model and the particle tracking code were taken from the in-flight icing code LEWICE [10]. A detailed description of the liquid film was proposed, including the effects of the water surface tension on the film. The film breaks up and individual rivulets are formed, separated by dry surface patches. An experimental test campaign was conducted to validate the numerical predictions [4]. Subsequent numerical model developments exploited these results [11–13]. Another relevant work on the modeling of hot-air anti-icing systems was led by Morency et al. and implemented in the ice accretion simulation code CANICE [11]. They deployed an integral method to solve the boundary layer. The air heat transfer coefficient was estimated using a momentum and heat transfer analogy [14]; the transition onset was estimated using Michel's classic correlation [15] and the turbulent boundary layer was assessed using the model developed by Ambrok [16]. Later on, Morency et al. [17] considered a finite difference numerical scheme to compute momentum, heat and mass balance around the airfoil to determine the air heat transfer coefficient. This procedure took into account both the laminar and turbulent boundary layer as well as transition one. The liquid film was modeled considering mass conservation in each control volume and then by computing the liquid film height using the momentum balance.

Silva et al. [18] developed a model for an electro-thermal IPS operating in anti-ice regime based on Messinger formulation of the ice accretion problem [19]. Mass and energy conservation equations are solved in each control

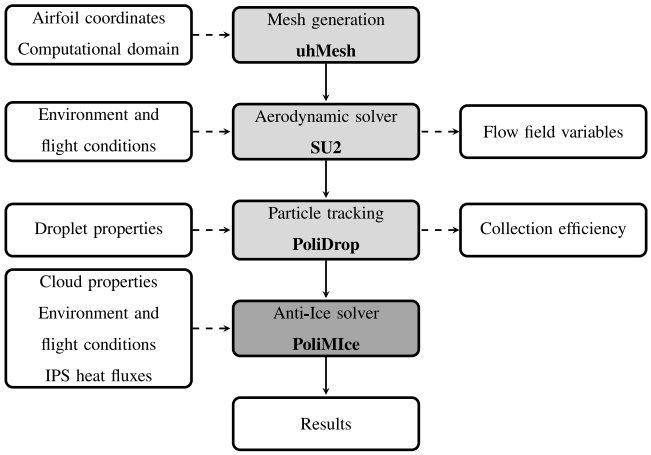

Fig. 1. Flowchart of the PoliMIce framework for an anti-ice simulation.

volume. The liquid film height was computed afterwards based on the water mass balance results. Later on, the authors implemented a numerical procedure to solve the integral equations of momentum and thermal boundary layers, considering a non-isothermal surface. In this way, laminar, turbulent and transition regimes could be accounted for. In later work, Silva et al. introduced an empirical transition model to predict the transition onset and the extension of the transition region [20]. Additionally, Bu et al. proposed an analogous model using a single energy balance in the liquid film, but including a freezing model [13].

In the present work, a model for an electro-thermal anti-ice system is proposed. Starting from the work by Silva et al. [18], the energy conservation laws for water and airfoil surface are solved. Moreover, the boundary layer model presented by Silva et al. [20] is used to determine the air heat transfer and skin friction coefficients.

In addition, an alternative liquid film model is studied. The model, based on lubrication theory, was proposed by Myers et al. [21]. The liquid film model is adapted here to the anti-ice problem in steady-state operation. The possibility to predict runback ice formations is included in the formulation of the problem along with a more robust evaporation model. Lastly, an alternative formulation based on Lagrangian polynomial interpolation was adopted to assess the water temperature within a control volume, to avoid the possibility of non-physical values. The model studied in this work is implemented in the PoliMIce software [22–24], an ice accretion simulation framework developed at Politecnico di Milano. In this work the capabilities of PoliMIce are extended by adding a new framework for the modeling of an electro-thermal IPS.

The present paper is organized as follows. In Section 1 an overview of anti-icing systems and current models were introduced. Section 2 contains a description of PoliMIce framework for anti-ice simulations. In Section 3 the numerical models studied in this work are described: thermodynamic, evaporation and liquid film. Section 4 contains a description of the reference experimental data used to validate the present code. In Section 5 the results of the test cases are presented.

2. PoliMIce simulation framework for anti-ice models

The main goal of an anti-ice simulation is to determine the distribution of water on the surface and to compute its thermodynamic phase, that is assessing whether it remains liquid, evaporates or freezes. Moreover, it is necessary to determine the temperature profile on the surface of the airfoil to ensure the integrity of the materials. To compute these quantities, energy and mass conservation equations are solved into control volumes on the airfoil surface. This is achieved through different modules that model physical features and evaluate the required parameters.

In an anti-ice simulation, it is necessary to first determine the flow field through an aerodynamic solver. The open-source code SU2 [25] was used. Then, the trajectories of supercooled droplets in the flow field are assessed by means of the Lagrangian particle tracking solver PoliDrop [26]. The distribution of water impinging on the surface of the airfoil is determined by evaluating the collection efficiency (β) that is defined as the ratio between the far-field area and the surface area enclosed by the same droplets trajectories. Lastly, the thermodynamic solver, which is the core of the software, reads the aerodynamic field and impinging variables and solves conservation laws to evaluate the surface temperature and water distribution and phase. Fig. 1 shows the simulation framework for an electro-thermal IPS in anti-ice conditions.

In the simulation of an anti-ice system, there are two fundamental aerodynamic parameters: the air heat transfer coefficient and the shear stress at the surface of the airfoil. The former is strictly related to the convective and evaporative heat fluxes, which are the main energy contributions to the energy balance. The latter is the main force that drives the liquid film over the airfoil surface and therefore it determines the height of the water layer. Thus, an accurate prediction of these quantities is crucial.

The evaluation of these parameters by means of a Navier–Stokes CFD simulation would require a computationally demanding iterative calculation. This would include CFD, particle tracking computations and the evaluation of the thermodynamic solver as the convective heat fluxes from the airfoil modify the aerodynamic temperature field. Therefore, the imposition of CFD boundary conditions on the airfoil surface would be strictly dependent on the liquid film thermodynamic problem. However, the thermodynamic problem relies on aerodynamic and impingement quantities. Therefore, an iterative calculation including CFD and particle tracking should be performed.

In this work, an Euler CFD simulation was performed to predict the velocity, pressure and temperature on the airfoil surface. Then h_{air} and C_f were computed by means of a boundary layer model using equations in the integral form [18] for both laminar and turbulent regimes. The transition region onset and extension were predicted by means of a model based on empirical observations presented in the work of Silva et al. [20]. In the transition region, the aerodynamic properties are computed as a linear combination of the laminar and turbulent ones.

3. Ice protection system modeling

The anti-ice solver moves from the model proposed by Silva et al. [18,20,27]. The core of the current anti-ice model is the solution of energy and mass conservation laws within control volumes on the airfoil surface. The energy conservation is enforced both on the airfoil surface and in the water layer. Both equations are coupled by the convective heat transfer between the surface and the water film.

The heating element of an electro-thermal IPS is a multilayered substratum composed of materials with different thermal behaviors. In this model, the substratum is considered as a unique material with an equivalent thermal conductivity. For this reason, the conduction is only considered in the curvilinear abscissa direction and not in the direction normal to the surface.

Moreover, mass conservation in the water layer is enforced by means of a simplification of the Navier–Stokes equations, that is the lubrication theory. The model proposed by Myers et al. [21] for ice accretion was adapted to the steady-state anti-ice model. The governing equation for the water motion is therefore a scalar transport equation depending only on the liquid film height. The velocity profile was evaluated as a function of the liquid film height and driving forces: shear stress and pressure gradient. Then, the mass fluxes were retrieved from these values and they were used for the evaluation of the liquid film enthalpy.

Due to the airflow over the solid surface, viscous forces generate a boundary layer, which interacts with the freestream flow and the water film. A schematic representation is depicted in Fig. 2. The shear stresses and the air heat transfer coefficient are fundamental to determine the liquid film motion and the heat transfer. They strongly depend on the boundary layer regime. In this work, the thermal and momentum boundary layers have been modeled based on the work by Silva et al. [18]. They allow to determine the boundary layer regime, the transition region extension and the values of skin friction and heat transfer coefficient. This is performed by solving the momentum and thermal boundary layer equations for both laminar and turbulent flows. In order to assess the local boundary layer regime, an empirical model was included [28], which only requires the specification of the turbulence intensity. This model was formulated for a flat plate geometry in a low-speed wind tunnel in which Reynolds numbers were in the range of a million. Due to the smooth and relatively low curvature of the airfoil, it was concluded that it was suitable to capture the physics of the problem at hand. However, it is noted that significant deviations could arise when considering flows with higher Reynolds numbers, large angles of attack or abrupt curvatures. This poses a limitation of this model since the experimental data available to validate alternative configurations are unavailable. To treat the transition region, the aerodynamic properties are computed as a linear combination of properties for turbulent and laminar regimes weighted by a normal cumulative distribution function. This function estimates the probability of the boundary layer to be turbulent at a certain position.

An important feature of an IPS model regards the capability of predicting the formation of runback ice in unprotected regions, which could greatly reduce flight safety. The model proposed by Silva et al. [18] does not include freezing terms and it is assumed that when the equilibrium temperature reaches the freezing temperature the incoming mass rate of water immediately freezes regardless of the incoming mass rate. Moreover, in the work by Bu et al. [13], a model for ice accretion was included and the mass of ice was externally computed and coupled with the energy conservation through an additional iterative step. If the water flows on the unprotected region and reaches the freezing temperature it is considered to start freezing until all the latent heat is released. In this work, a temperature-dependent freezing heat flux has been included into the energy conservation for the liquid film, the detailed procedure to determine the freezing mass rate and the freezing heat flux is explained in the Section 3.1.

The anti-ice solver, then, contains multiple models that are loosely coupled one to another. This leads to a quite complex numerical approach that needs to account for the influence between the models. In this chapter, all the novelties introduced in the present work, along with the numerical implementation in the software PoliMIce are presented.

3.1. Conservation equations with freezing terms

As stated before, the anti-ice solver is based on the solution of mass and energy conservation laws. In this section, the energy conservation laws are presented. The mass conservation law is linked to the liquid film model that is discussed in the next section.

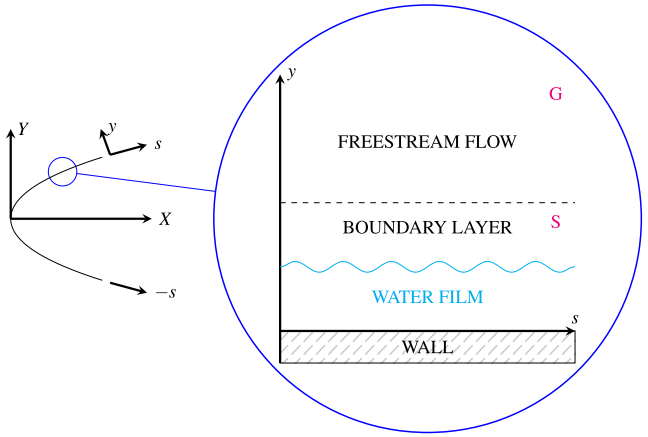

Fig. 2. Airfoil reference system with a detail of the different zones of the physical problem. Region S is the region just above the liquid film which contains saturated vapor in equilibrium with the liquid phase. Region G represents the flow outside of the boundary layer where the vapor concentration is smaller.

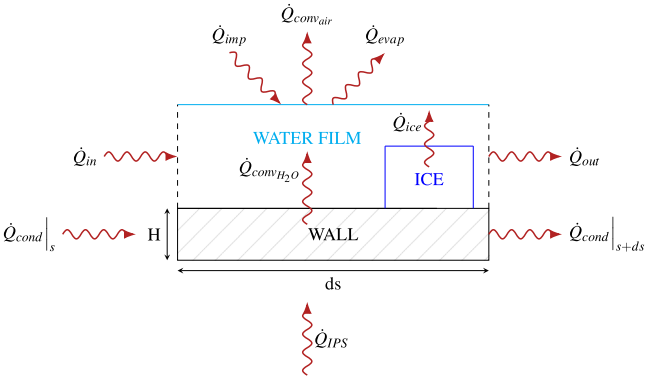

Fig. 3. Contributions to energy conservation in a finite volume.

The energy conservation law is enforced both in the water film and on the surface of the airfoil by considering the incoming and outgoing heat fluxes in each control volume, as shown in Fig. 3. The two equations, in the unknowns T_{wall} and T_{H_2O}, are linked through the water convective heat flux. The energy conservation applied on the airfoil surface takes into account only the conduction in the direction parallel to the surface. Due to the small thickness of the heating elements, conduction in the normal direction to the surface has been neglected. The equivalent thermal conductivity of the substratum can be estimated by means of an electrical analogy, considering the thermal resistance of the materials forming the heating element in parallel, from the heater to the external surface at the top.

The wetness factor F represents the wet area fraction in the finite volume: $F = 1$ if the surface of the element is fully wet, $F = 0$ if the surface is fully dry, $0 < F < 1$ if the element is partially wet. Through this, it is possible to determine whether the heat is transferred by convection only to water, air or both. As it can be seen in Fig. 3, energy conservation on the airfoil surface yields:

$$\dot{Q}_{cond} + \dot{Q}_{IPS} - (1 - F)\ \dot{Q}_{conv_{air}} - F\ \dot{Q}_{conv_{H_2O}} = 0, \tag{1}$$

where the first term is associated to conduction in the solid surface:

$$\dot{Q}_{cond} = A\,\frac{d}{ds}\left(k_{wall}\,H\,\frac{dT_{wall}}{ds}\right), \tag{2}$$

where s is the curvilinear abscissa, k_{wall} is the equivalent thermal conductivity of the wall and H is its thickness. $\dot{Q}_{IPS}$ is the heat provided by each heater. Then, there is heat associated to convection from wall to air:

$$\dot{Q}_{conv_{air}} = A\,h_{air}\ (T_{wall} - T_{rec}), \tag{3}$$

and the convective heat from wall to water:

$$\dot{Q}_{conv_{H_2O}} = A\,h_{H_2O}\ \left(T_{wall} - T_{H_2O}\right). \tag{4}$$

These two terms are multiplied by $(1-F)$ and F respectively, to account for air or water convection depending on whether the considered control volume is fully dry, partially wet or fully wet.

T_{rec} is the recovery temperature and takes into account the effects of aerodynamic heating in the boundary layer. It is defined as:

$$T_{rec} = (1-r)\ T_e + r\ T_0, \tag{5}$$

where T_e is the local temperature outside the boundary layer, T_0 the stagnation temperature and r the recovery factor. The latter depends on the boundary layer regime and it is assumed to be $\sqrt{Pr}$ for laminar flows and $\sqrt[3]{Pr}$ for turbulent flows. In this work $Pr \approx 0.71$ which is an acceptable value for an ideal gas for a wide range of temperatures.

Within the liquid film, again the energy conservation is determined by taking into account all the heat fluxes within a given volume, as shown in Fig. 3. The conservation equation is reported as:

$$F\ \dot{Q}_{conv_{air}} + F\ \dot{Q}_{conv_{H_2O}} + \dot{Q}_{in} - \dot{Q}_{out} + \dot{Q}_{imp} - \dot{Q}_{evap} + \dot{Q}_{ice} = 0. \tag{6}$$

The first heat contribution is the convective heat from water to air:

$$\dot{Q}_{conv_{air}} = A\ h_{air}\ \left(T_{rec} - T_{H_2O}\right); \tag{7}$$

then there is the convective heat from wall to water:

$$\dot{Q}_{conv_{H_2O}} = A\ h_{H_2O}\ \left(T_{wall} - T_{H_2O}\right); \tag{8}$$

$\dot{Q}_{in}$ is the sensible heat associated to the water entering the control volume:

$$\dot{Q}_{in} = \dot{m}_{in}\ c_{p_{H_2O}}\ \left(T_{in} - T_{ref}\right); \tag{9}$$

$\dot{Q}_{out}$ is the sensible heat associated to the water leaving the control volume:

$$\dot{Q}_{out} = \dot{m}_{out}\ c_{p_{H_2O}}\ \left(T_{out} - T_{ref}\right); \tag{10}$$

$\dot{Q}_{imp}$ is the heat due to the impinging droplets, including both the kinetic and sensible heat contributions:

$$\dot{Q}_{imp} = \dot{m}_{imp}\ \left[c_{p_{H_2O}}\ \left(T_{imp} - T_{ref}\right) + \frac{V_{imp}^2}{2}\right]; \tag{11}$$

$\dot{Q}_{evap}$ is the sensible and latent heat associated to evaporation:

$$\dot{Q}_{evap} = \dot{m}_{evap}\ \left[i_{l-v} + c_{p_{H_2O}}\ \left(T_{H_2O} - T_{ref}\right)\right]; \tag{12}$$

last $\dot{Q}_{ice}$ is the sensible and latent heat associated to icing:

$$\dot{Q}_{ice} = \dot{m}_{ice}\ \left[i_{l-s} + c_{p_{H_2O}}\ \left(T_{H_2O} - T_{ref}\right)\right]. \tag{13}$$

$T_{ref} = 273.15\,\mathrm{K}$ is the reference temperature for computing the sensible enthalpy. The temperatures T_{in} and T_{out} are the temperatures of the incoming and outgoing water respectively. The convective heat transfer coefficient of water links the water film model to the thermodynamics of the problem. It is calculated through the Chilton and Colburn analogy which directly relates the heat transfer, mass transfer and friction coefficients and permits the prediction of an unknown transfer coefficient when one of the others is known. Its definition is reported below:

$$St = \frac{C_f}{2}\ Pr^{-2/3}. \tag{14}$$

Substituting the definition of Stanton number St, the heat transfer coefficient of water is obtained as follows:

$$h_{H_2O} = \frac{1}{2}\ \rho_{H_2O}\ u_f(s, h_f(s))\ c_{p_{H_2O}}\ C_f\ Pr_{H_2O}^{-2/3}. \tag{15}$$

In this work, freezing is assumed to occur in a range of 0.05 K around the fusion temperature (273.15 K). The rate of ice formation is dependent on the incoming water mass and the equilibrium temperature. If the equilibrium temperature is lower or higher than the fusion temperature bounds respectively, then all or none of the water will freeze. For water equilibrium temperatures within the freezing bounds, that is 273.15 ± 0.05 K, the freezing mass rate depends on the normalized difference between the temperature to the lower bound. Once the freezing mass rate is known, the freezing heat flux can be retrieved as shown in Eq. (13).

3.2. Liquid film model

The model used in this work is based on a simplification of the Navier–Stokes equations for an incompressible flow, that is the lubrication theory or long-wave approximation [21]. This model was also deployed for icing applications in the

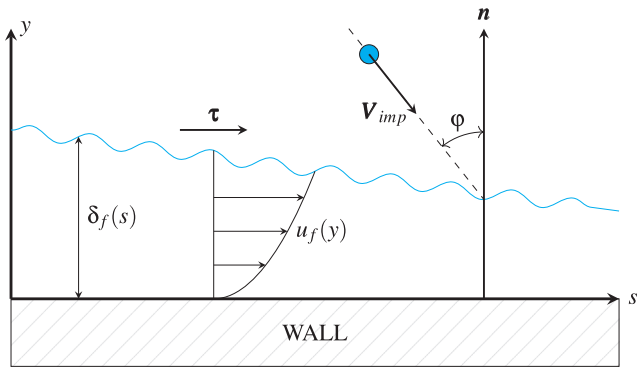

Fig. 4. Water film detail. The parabolic velocity profile in the liquid film is highlighted along with the two driving forces: the wall shear stress τ and the momentum per unit area from incoming water droplets.

work by Beaugendre et al. [29] and in the work by Chauvin et al. [30]. This approximation is valid if the liquid film can be considered thin and the flow regime laminar. Being H the characteristic depth and L the characteristic length in the direction of the flow, two conditions must be satisfied: $\frac{H}{L} \ll 1$ and $\frac{uL}{\nu}\frac{H}{L} \ll 1$. In this way, by applying proper boundary conditions, the system is reduced to a single scalar equation, which is only dependent on the height of the liquid film:

$$\frac{\partial \delta_f \bar{u}_f\left(\delta_f, s\right)}{\partial s} = \frac{\dot{m}''_{imp} - \dot{m}''_{evap} - \dot{m}''_{ice}}{\rho_{\mathrm{H_2O}}}, \tag{16}$$

where $\bar{u}_f\left(\delta_f, s\right)$ is the liquid film bulk velocity that is obtained from the momentum balance by imposing no slip boundary conditions at the wall and continuity of stresses at the air–water interface. For slow water speed compared to airflow, the Navier–Stokes solution is approximately the same as the one over a stationary wall [11]. Thus the shear force is the sum of the wall shear stress τ and the momentum per unit area from incoming water droplets, as can be seen from Fig. 4. The obtained parabolic velocity profile is then averaged along the height of the film leading to:

$$\begin{aligned}\bar{u}_f\left(\delta_f, s\right) &= \frac{1}{\delta_f}\int_0^{\delta_f} u_f(s,y)dy \\ &= \frac{1}{6\,\mu_{\mathrm{H_2O}}}\frac{dp_e}{ds}\delta_f^2 + \frac{1}{2\,\mu_{\mathrm{H_2O}}}\left(\tau + \dot{m}''_{imp}V_{imp}\sin(\varphi) - \delta_f\frac{dp_e}{ds}\right)\delta_f.\end{aligned} \tag{17}$$

Eq. (16) is then discretized using a finite volume approach with an upwind scheme. Once the water film height δ_f is obtained for the corresponding element, the outflow mass of water is retrieved using the definition of mass flow rate $\dot{m} = \rho AV$, leading to:

$$\dot{m}_{out} = \rho_{\mathrm{H_2O}}\delta_f\bar{u}_f\left(\delta_f\right), \tag{18}$$

while the inflow mass is retrieved by imposing that it must be equal to the mass flowing out from the neighboring control volume. Once $\dot{m}_{in}$ and $\dot{m}_{out}$ are known they can be used in the energy conservation equation (6). Moreover, the obtained film height is used to evaluate the heat transfer coefficient of water (15). The main advantage of this liquid film model, with respect to an element-wise mass balance, is that it can be easily extended to the unsteady problem and coupled with more complex icing models in order to better capture more complex runback-ice shapes.

3.3. Computation of the evaporating mass rate

For the computation of the mass rate of evaporation, it is assumed there is a region just above the liquid film (region S) which contains saturated vapor. The vapor is in equilibrium with the liquid phase and therefore they are at the same temperature. The concentration of vapor in the freestream flow (region G) is smaller since its temperature is significantly lower. Both regions are presented in Fig. 2. Therefore, a vapor concentration gradient is present and a mass diffusion process takes place. Water vapor is transported from the region S to the freestream flow in region G, namely evaporation. The evaporative mass rate can be estimated through the Fick's law of mass diffusion, that is:

$$\dot{m}''_{evap} = h_m\left[\rho_{sat_{\mathrm{H_2O}_S}} - \rho_{\mathrm{H_2O}_G}\right], \tag{19}$$

where h_m is the mass transfer coefficient, $\rho_{\mathrm{H_2O}_i}$ corresponds to the mass of water vapor per unit volume at the location i (either G or S) and subscript *sat* describes saturation. The mass transfer coefficient h_m is derived from the heat and mass

transfer analogy, namely the Chilton and Collburn analogy, which reads:

$$\frac{Nu}{Pr^{\frac{1}{3}}} = \frac{Sh}{Sc^{\frac{1}{3}}}, \tag{20}$$

where Sh, Sc and Nua are Sherwood, Schmidt and Nusselt non-dimensional numbers respectively. Then, using the relation (20), h_m can be computed as:

$$h_m = h_{air} \frac{1}{\rho\ C_p\ Le^{\frac{2}{3}}}. \tag{21}$$

The concentration of water vapor $\rho_{H_2O_i}$ is computed through the ideal gas law, assuming that water vapor is an ideal gas, that is:

$$\rho_{H_2O_i} = \frac{p_{H_2O_i}}{\mathfrak{M}_{H_2O}\ \mathcal{R}\ T_i}. \tag{22}$$

At the location S, the water is assumed to be saturated and therefore, the saturation pressure $p_{sat_{H_2O_i}}$ must be evaluated. It is only dependent on the temperature of the water vapor and not on the pressure of the air, as stated in the Goff–Gratch correlation [31]. This correlation is used in the present work for the computation of $p_{sat_{H_2O_i}}$.

The heat and mass transfer analogy is commonly deployed in icing models to evaluate the evaporative mass flux, for instance, in the work of Wright et al. [32]. This formulation is selected in the present work because $\dot{m}''_{evap}$ is continuous for the ranges of values of interest for the relevant thermodynamic properties. These include the freestream pressure and the local temperature of the saturated vapor. The continuity cannot be assured for other formulations such as the alternative proposed by Silva et al. [20]. Therefore this formulation is more robust and versatile.

3.4. Estimation of outflow enthalpy of the runback water

The variation of enthalpy of the liquid film across a control volume is computed by estimating the temperature variations. In the work of Silva et al. [20], the temperature of water within a control volume is estimated by assuming the average of the incoming and outgoing temperatures

$$T_{H_2O} = \frac{T_{in} + T_{out}}{2}. \tag{23}$$

This formulation does not allow to account for the temperature variation in the downstream control volume and for the size of the control volume. Significant variations of the water temperature downstream can lead to nonphysical values of T_{out} and to a non-physical oscillation of T_{H_2O}. In this work, an alternative formulation is proposed, based on a Lagrangian polynomial interpolation. For each i^{th} element of the surface mesh, the temperature on three points, indicated with the subscript j, are considered: the temperature of the incoming water $T_{in,i}$ (T_1), the water temperature in the control volume $T_{H_2O,i}$ (T_2) and the water temperature in the next control volume $T_{H_2O,k}$ (T_3), according to the flow direction of the liquid film. The interpolation points are shown in Fig. 5. Furthermore, the curvilinear abscissa values (s_j) for each location are accounted for, which was not the case on the initial formulation. Consequently, the temperature of the outgoing water can be obtained as:

$$T_{out}(s) = \sum_{j=1}^{3} T_j L_j(s), \tag{24}$$

where L_j correspond to the Lagrange polynomials that can be computed as:

$$L_j(s) = \prod_{\substack{m \neq j \\ 1 \leq m \leq 3}} \frac{s - s_m}{s_j - s_m}. \tag{25}$$

Due to the iterative nature of the calculation, the temperature of the neighboring element can be taken from the previous iteration.

3.5. Thermal conduction approximation

Conduction in the multilayered substratum has been approximated by means of a unique layer with equivalent thermal conductivity k_{wall}. This approach has been also deployed in the works of Silva et al. [20] and Bu et al. [13]. To compute such, only the layers above the heaters are considered because the thermal conductivity of the bottom materials is low. Consequently, it is assumed that all the heat generated is transferred towards the external surface and not to the inner chamber of the airfoil. Three different materials are positioned parallel to the direction of conduction whose thermal

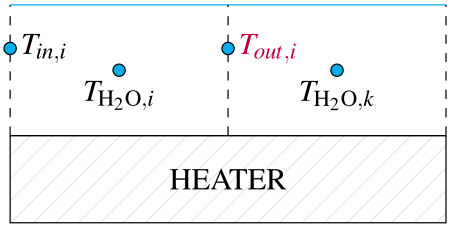

Fig. 5. Interpolation points used in the computation of T_{out} of the ith control volume: the temperature of the incoming water $T_{in,i}$, the water temperature in the control volume $T_{H_2O,i}$ and the water temperature in the next control volume $T_{H_2O,k}$, according to the flow direction of the liquid film.

properties and thicknesses are reported in Table 1. The electrical analogy of resistors is applied. Each material i is modeled as a resistance to conduction R_i whose magnitude is computed as:

$$R_i = \frac{t_i}{k_i A_i'}, \tag{26}$$

where t_i is the thickness of a layer and A_i' is the cross section of the material in which heat is conducted. The three resistances corresponding to each of the layers of the materials are positioned in parallel. After, the equivalent thermal resistance is computed as follows:

$$R_{eq} = \frac{\prod_{j=1}^{3} R_i}{\sum_{j=1}^{3} R_i}. \tag{27}$$

Finally, the equivalent thermal conductivity can be computed directly from Eq. (26). It is noted that there are more sophisticated conduction models available in the open literature, specially for de-ice applications solving the heat equation in the multilayered substratum, such as in the work of Reid et al. [33].

3.6. Numerical solution of the IPS model

The anti-ice solver implemented in PoliMIce takes as inputs the results of the Euler CFD simulation and the collection efficiency from the particle tracking.

Then the stagnation point is determined as the point of minimum velocity. From here, the boundary layer computation is performed to evaluate values of the shear stress and the heat transfer coefficient, for a fixed temperature profile (fixed T_{wall} and T_{rec}). Once these quantities are retrieved, the conservation equations for the airfoil surface and the water film are resolved for each element of the surface mesh, starting from the elements surrounding the stagnation point, where the inflow quantities are set to zero. For each element, Eqs. (1), (6) and (16) are solved. These equations are non-linear as h_{air} depends on T_{wall} and h_{H_2O} depends on T_{H_2O}. Moreover, h_{H_2O} depends on the water film velocity $\bar{u}\left(h_f\right)$ and the evaporative mass flux needed in Eq. (16) depends on T_{H_2O}. From Eq. (1), T_{wall} can be expressed as a function of T_{H_2O}. Therefore, the only unknown is T_{H_2O} and the problem is solved by means of a bisection method applied to energy conservation in the water layer. Eq. (6) is solved iteratively until the absolute value of the residual is below a given tolerance, 10^{-6} here. These computations are repeated in every finite volume, from the stagnation point to trailing edge on both sides. In this way, the temperature distribution on the airfoil surface T_{wall}, the temperature of the water film and the runback mass fluxes are obtained. The recovery temperature T_{rec} is updated as it depends on the boundary layer regime. The loop is repeated until the maximum value among all elements of the difference between two subsequent iterations of the surface temperature T_{wall} is lower then a given tolerance: $\max\left|T^{it}_{wall,i} - T^{it-1}_{wall,i}\right| < \varepsilon$, where $\varepsilon = 10^{-2}$. The flowchart in Fig. 6 summarizes the numerical implementation of the model. To clarify, the iterations of the bisection method are indicated with it_b while the iterations of the main loop with it. The function $F(T_{H_2O})$ indicates the energy conservation law on the liquid film.

4. Reference test cases

The described Ice Protection System model is tested in three different anti-ice conditions from the experimental work of Al-Khalil et al. [4]. They have been widely used to validate numerical models in literature. The geometry used in the test was an extruded NACA0012 profile of 0.914 m chord and 1.828 m span. As shown in Fig. 7, the airfoil was equipped with seven heaters controlled separately to provide different thermal heat fluxes. The protected area was 0.197 m in the streamwise direction. Every heater is composed by several layers: the metal heating element is embedded between two layers of insulating material. Table 1 presents the composition of the heaters with thermal conductivity and other properties of the materials. From inside to the external surface the layers are: silicone foam thermal insulation, fiberglass/epoxy composite, an elastomer layer, heater resistance, another elastomer layer, and an erosion shield [4].

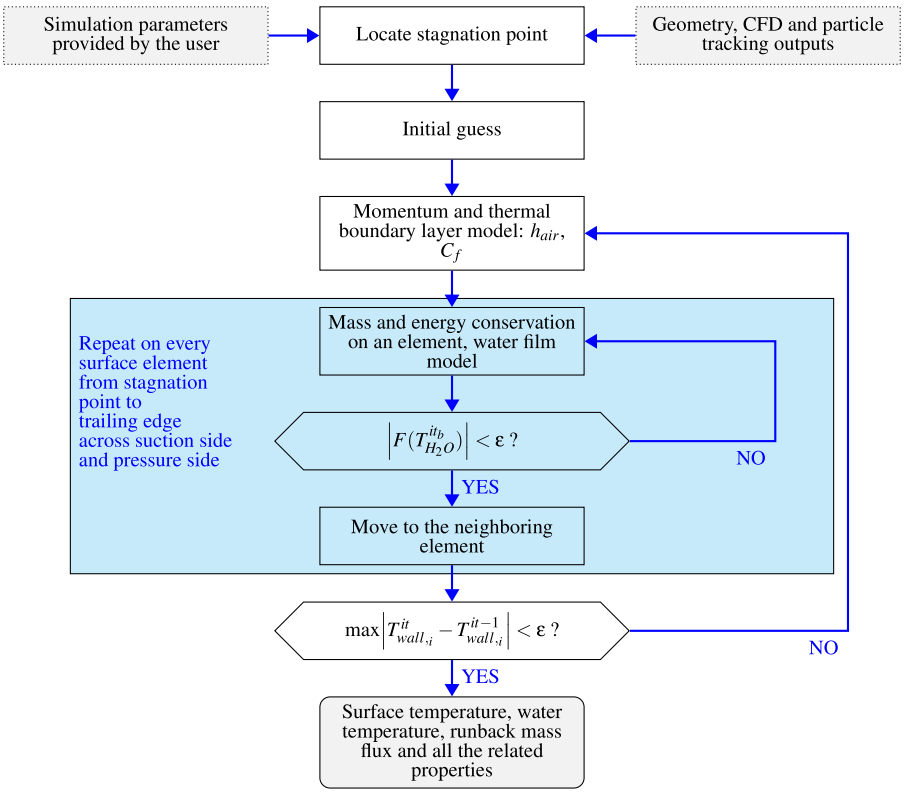

Fig. 6. Flowchart of the numerical implementation of the model.

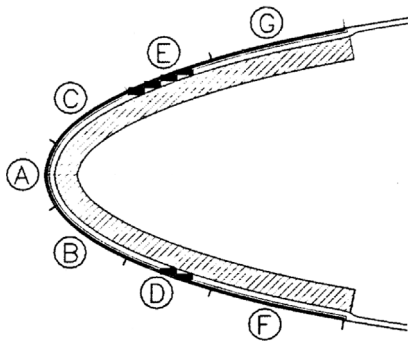

Fig. 7. Airfoil leading edge and heated zones [4].

Table 1
Heaters layers with material properties, from Al-Khalil et al. [4].

MATERIAL	$k\left[\frac{W}{mK}\right]$	$\rho\left[\frac{kg}{m^3}\right]$	$c_p\left[\frac{J}{kgK}\right]$	t [mm]
Heating Element (Alloy 90)	41.02	8906.26	385.19	0.03
Erosion Shield (SS 301 HH)	16.27	8025.25	502.42	0.2
Elastomer (Cox 4300)	0.256	1384	1256.04 ± 125.6	0.26
Fiberglass/Epoxy Composite	0.294	1794.07	1570.05	0.89
Silicone Foam Insulation	0.121	648.25	1130.44 ± 125.6	3.43

As discussed in Section 3.5 in the numerical simulation, all the layers are considered as a single one and the equivalent thermal conductivity is equal to 4.7 W/m. Table 2 presents the start and end position of the heaters along with the corresponding heat fluxes allocated in each heater for each test case. Due to a manufacturing problem [4], the heaters

Table 2
Heater locations on the airfoil and heat fluxes for test cases 22A, 67A, 67B.

	Position		$\dot{q}''_{IPS}$ (kW/m^2)		
Heater	Start ($\frac{s}{c}$)	End ($\frac{s}{c}$)	22A	67A	67B
F	−0.1024	−0.0607	9.92	20.15	8.37
D	−0.0607	−0.0329	10.23	21.70	11.94
B	−0.0329	−0.0051	32.55	32.55	10.85
A	−0.0051	0.0157	46.50	43.40	15.19
C	0.0157	0.0435	18.60	26.35	9.92
E	0.0435	0.0713	6.98	18.60	12.87
G	0.0713	0.1129	10.23	18.60	8.68

Table 3
Simulation parameters for test case 22A, 67A and 67B [4].

	22A	67A	67B
α (°)	0°	0°	0°
V_∞ (m/s)	44.7	89.4	89.4
T_∞ (K)	265.45	251.35	251.35
P_∞ (Pa)	90 000	90 000	90 000
MVD (μm)	20	20	20
LWC (g/m^3)	0.78	0.55	0.55

were not placed symmetrically over the profile. An estimated shift of 0.0145 m towards the suction side was reported by the authors. This lead to asymmetrical results even if the flow and the airfoil are symmetric.

To assess the validity of the model implemented in PoliMIce, three test cases were selected from the experimental campaign: 22A, 67A and 67B. They have been chosen because reference data are available from the validation of several numerical codes: ANTICE [4] and the ones developed by Silva et al. [27] and Bu et al. [13]. In this way, the predicting capabilities of the new model can be compared with other numerical models, as well as to experimental results.

The runback water mass flux $\dot{m}_{H_2O}$, the surface temperature on the airfoil T_{wall}, the convective heat transfer coefficient h_{air} and the global heat transfer coefficient U are analyzed for each test case. The global heat transfer coefficient was introduced in the work by Al-Khalil et al. [4] to compare numerical results with experimental data. The exact definition is not reported, but due to its experimental nature, it was calculated with experimental readings. As a consequence, it includes the temperature difference between the measured surface temperatures and the far-field temperature. It is also assumed to be proportional to the heat flux measured by several gauges placed underneath the outer surface. In the present simulations, the heat flux is assumed to be equal to $\dot{q}''_{IPS}$. Therefore, the global heat transfer coefficient is computed as:

$$U = \begin{cases} \frac{\dot{q}''_{IPS}}{\Delta T} & \text{if } F > 0 \\ h_{air} & \text{if } F = 0, \end{cases} \tag{28}$$

where ΔT represents the temperature difference between the far-field and surface temperatures. Additionally, and to compare with the computational reference results, the value of the global heat transfer coefficient is evaluated with ΔT equal to the temperature difference between the local recovery and surface temperatures.

The three selected test cases are representative of different anti-ice operating modes. Test case 67B is a running wet condition, 67A and 22A are in fully evaporative condition. In 22A full evaporation is obtained rapidly and protected parts are exposed to airflow. Table 3 presents the icing tunnel test conditions of the three test cases, while the heat fluxes provided by each heater are shown in Table 2. The heat fluxes set during the experimental campaign were chosen considering the amount of water that impinges on the airfoil. Due to the geometry of the test case, intuitively, a higher value of the heat flux would be needed close to the stagnation point. The heat fluxes are then decreased as moving further away from the leading edge. The turbulence level Tu, necessary for the calculation of the boundary layer transition, has been set to 3.1% for test case 22A, 1.9% for 67A and 3.0% for 67B as it was suggested by Silva et al. in [20].

A description of the layout and instrumentation deployed for the experimental test cases is presented in [34], together with the experimental uncertainties. The uncertainties considered include position uncertainty, data acquisition process and sensors inherent accuracy. These uncertainties are reported to be dependent on the heat flux. Then, the uncertainties for three nominal fluxes are estimated, which present a linear trend. The exact values have been linearly interpolated here from those presented in Ref. [34]. As for the global heat transfer coefficient, the heat flux reading from the heat flux gauge is required. The uncertainty of this measurement as well as the specifications of the gauge were not reported. Nevertheless, this uncertainty is expected to be large, due to the assumptions undertaken. Following Ref. [34], the thermal source is positioned underneath the heater and the outward heat flux is estimated to be twenty times larger [34]. This is because the thermal resistance downwards is significantly larger. In this work, it is expected that the uncertainty of the global heat transfer coefficient, which includes the measurements of the heat fluxes and temperature readings, is in the range of 15%. However, it is acknowledged that further work should be conducted to further characterize this uncertainty.

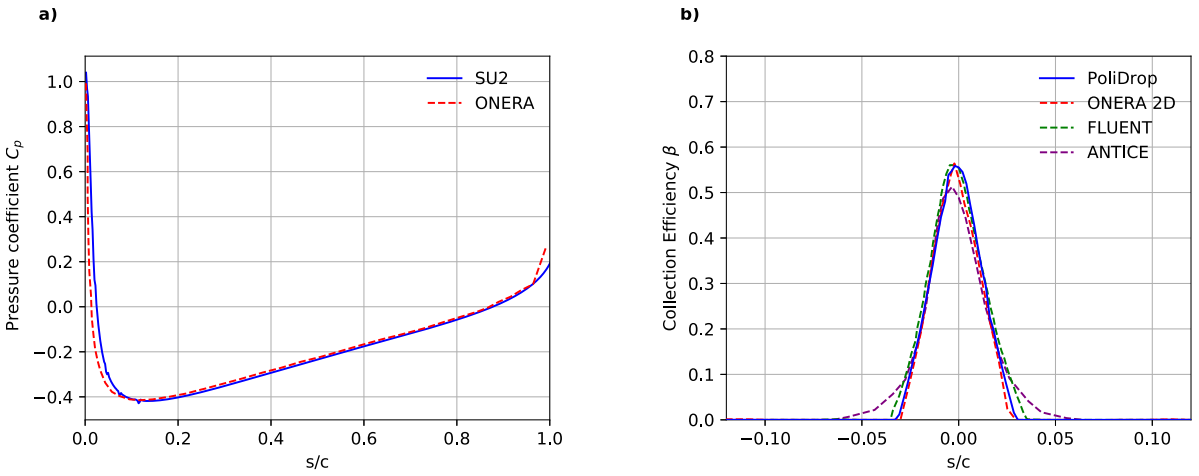

Fig. 8. (a) Computed pressure coefficient for the test case 22A obtained by means of SU2 and by Silva et al. [20] using the ONERA software. (b) Water collection efficiency on the surface of the airfoil computed with PoliDrop [26] and by Silva et al. [20] by means of the ONERA software, Bu et al. [13] using FLUENT and by Al-Kalil et al. using the code ANTICE [4].

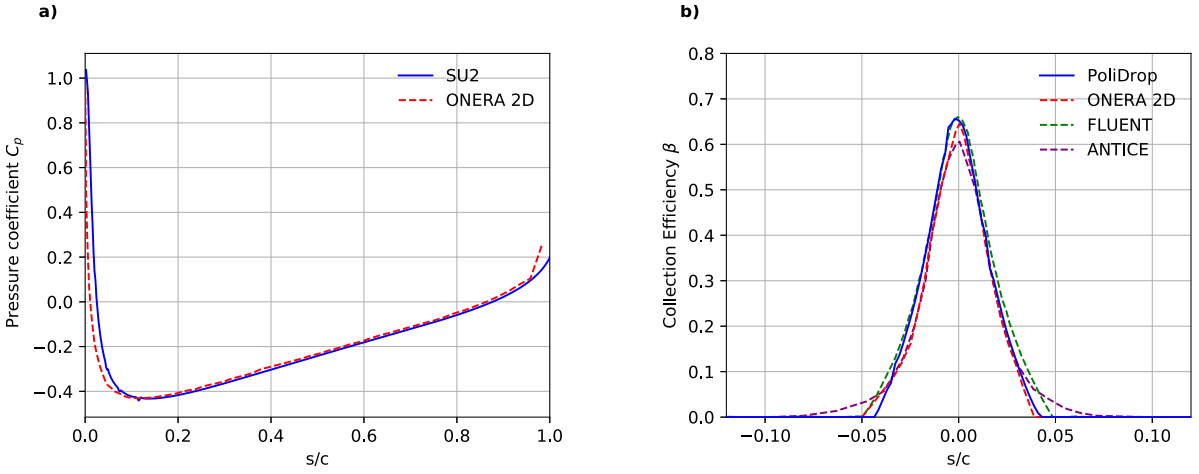

Fig. 9. (a) Computed pressure coefficient for the test cases 67A and 67B obtained by means of SU2 and by Silva et al. [20] using the ONERA software. (b) Water collection efficiency on the surface of the airfoil computed with PoliDrop [26] and by Silva et al. [20] by means of the ONERA software, Bu et al. [13] using FLUENT and by Al-Kalil et al. using the code ANTICE [4].

5. Results and discussion

The results obtained with PoliMIce for the three test cases are presented and compared against experimental data from Al-Khalil et al. [4] and against numerical results provided by Silva et al. [20], Bu et al. [13] and using the code ANTICE [4].

In this work SU2 was used to perform Euler simulations and the convective fluxes were solved with the Roe numerical method using a second order upwind scheme [35] with no slope limiter. Fig. 8(a) shows the pressure coefficient (C_P) obtained with SU2 for test case 22A and Fig. 9(a) the C_P for the test cases 67A and 67B. For these two test cases, the environmental conditions are the same. In these two plots, the x axis is the curvilinear abscissa normalized by the chord, namely s/c. The value $s/c = 0$ corresponds to the leading edge while $s/c = 1$ is the trailing edge. The C_P is symmetrical in both cases as it is expected for a symmetric airfoil with zero angle of attack. In both cases, it is compared with the one obtained with the software ONERA 2D by Silva et al. [27], showing good agreement. Figs. 8(b) and 9(b) present respectively the collection efficiency obtained by means of PoliDrop for the cases 22A and 67A and 67B. In both figures, the obtained results are compared to those obtained by Al-Khalil et al. [4], Silva et al. [27], and Bu et al. [13].

In the following plots, the reference system is the one presented in Fig. 2.

The surface temperature profiles, runback water mass flux, convective and overall heat transfer coefficient obtained with PoliMIce, along with reference experimental data from Al-Khalil et al. [4] and numerical reference results [4,20,13], are shown in Fig. 10 for test case 22A, in Fig. 11 for test case 67A and in Fig. 12 for 67B.

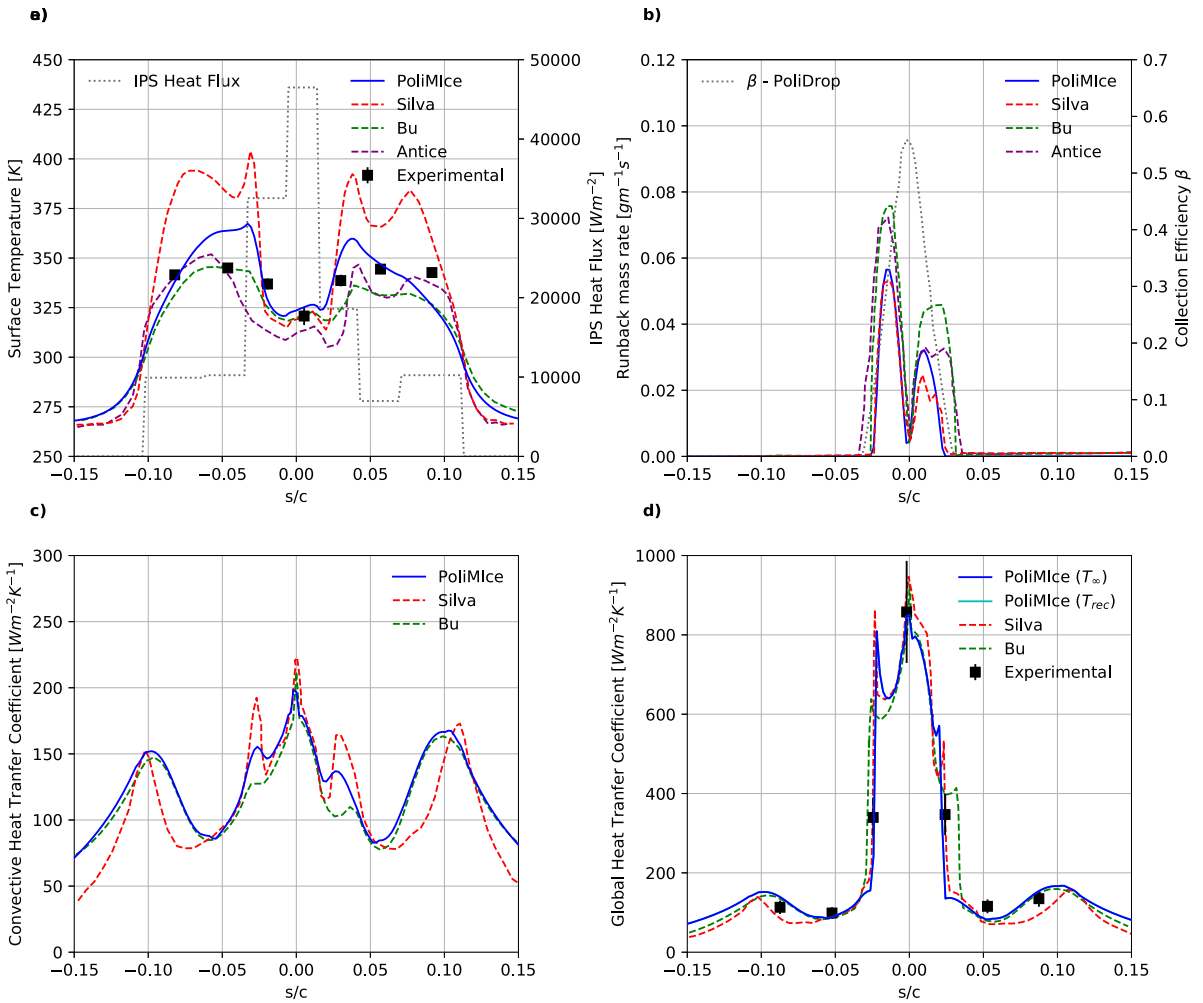

Fig. 10. Results for the test case 22A compared with experimental results from [4] and previous simulations presented in [20,13]. In figure (a), the temperature at the surface of the airfoil is depicted. Figure (b) shows the average runback water mass flowing at the surface of the airfoil. In figure (c), the convective heat transfer coefficient obtained is presented. In picture (d) the overall heat transfer coefficient is shown.

For test case 22A, the results obtained with PoliMIce show good agreement with reference data. Furthermore, it can be seen there is an agreement in the predictions by all the numerical codes. Fig. 10(a) presents the surface temperature on the airfoil. It can be noticed that T_{wall} is lower in the region closer to the stagnation point and increases rapidly after the runback water limits. Near the leading edge, most of the heat is used to evaporate water or increase its enthalpy. Downstream the runback water limits there is an increase in the temperature because the surface is fully dry and the heat released by the heaters significantly raises the surface temperature. Fig. 10(b) presents the runback water mass flux. The limits of the liquid film are very close to the limits of the collection efficiency and it is a consequence of the IPS working in fully-evaporative conditions: the impinged water evaporates before reaching the end of the protected region. The convective and the overall heat transfer coefficients are presented in Figs. 10(c) and 10(d) respectively. It can be seen that the results obtained with PoliMIce show good agreement with reference results. With regards to the convective heat transfer coefficient, there is an agreement with the three plots presented. This was expected because the three numerical models include the same boundary layer model. There are small differences in the prediction of the transition onsets and offsets. This could be due to differences in results obtained by different simulation frameworks, by the numerical methods used for integration and derivation, by variations on model parameters or by differences on the selected temperatures to compute the air properties in the boundary layer. With respect to experimental data, the peak position and value are well captured, as well as the overall trend. Due to the direct exposure of heaters to air and the consequent temperature rise, part of the heat is conducted through the solid and it is taken by the liquid film increasing $\dot{q}''_{IPS}$. This is causing the second peak on the global heat transfer coefficient presented in Fig. 10(d) at around $s/c = -0.025$.

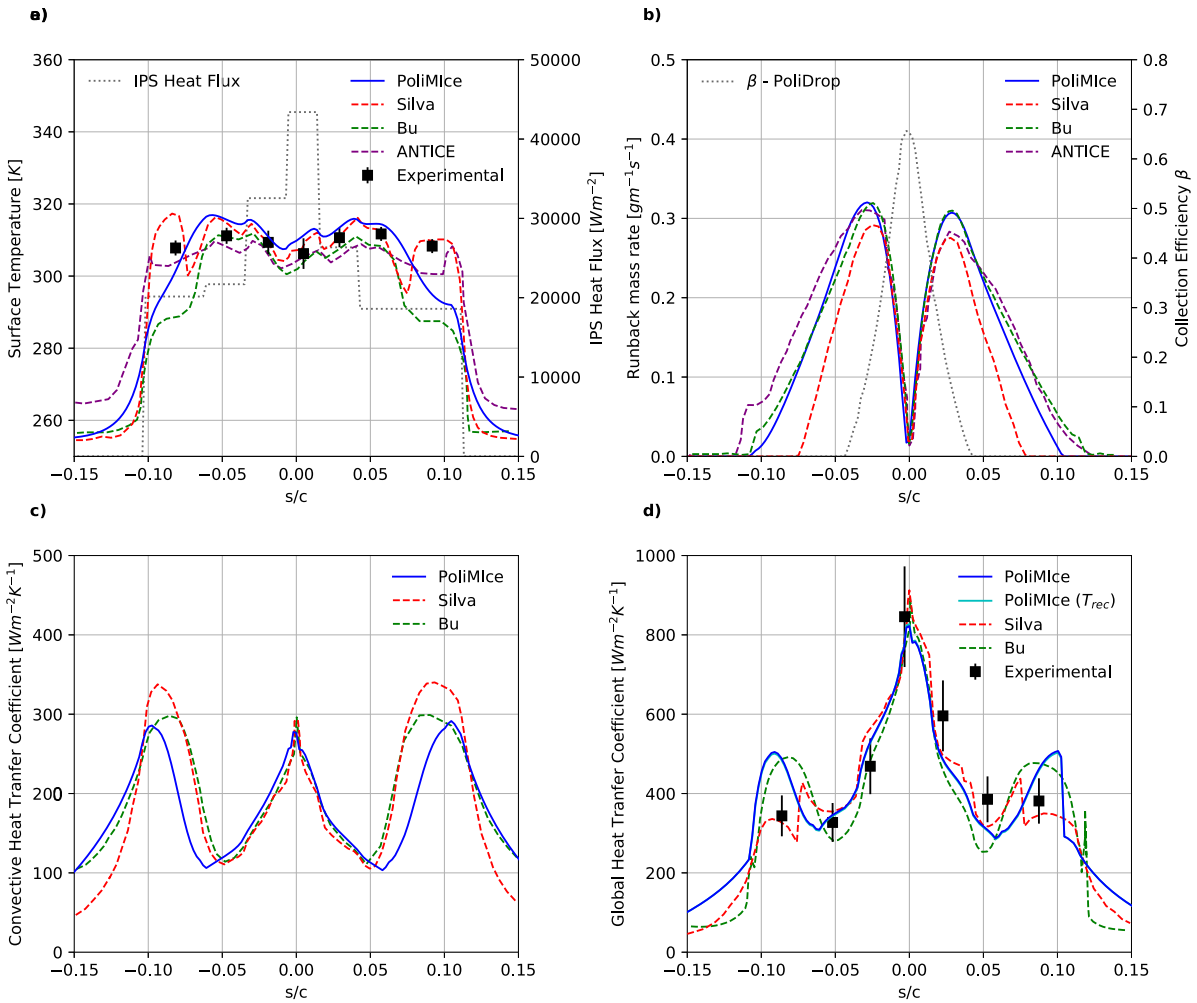

Fig. 11. Results for the testcase 67A compared with experimental results from [4] and previous simulations presented in [20,13]. In figure (a), the temperature at the surface of the airfoil is depicted. Figure (b) shows the average runback water mass flowing at the surface of the airfoil. In figure (c), the convective heat transfer coefficient obtained is presented. In figure (d) the overall heat transfer coefficient is shown.

These results confirm that this selection of heat fluxes for the environmental and flight properties leads to a fully-evaporative anti-ice operation. It is a very safe condition but also very energy consuming: the runback water is evaporated before the end of the protected region and this requires a high heating power.

Figs. 11(a) and 11(b) present the surface temperature and the average runback water mass flowing at the surface of the airfoil respectively for test case 67A. For both quantities, the results obtained by means of PoliMIce show good agreement with reference results, especially with the ones presented by Bu et al. [13]. As it was expected, the surface temperature is higher where the heaters are placed. A large drop in the temperature below the freezing temperature is located at the protected region limits. This is due to the increase in the heat transfer coefficient caused by the transition, which increases the convective losses. This could lead to the formation of runback ice if exposure is extended, also because the accuracy of the model is limited and there might be discrepancies between the model and reality. As it happened for test case 22A, the surface temperature at the stagnation point is lower despite the larger heat fluxes. This is caused by the large amount of water that impinges on this region and most of the heat is used to warm up the impinging droplets. Contrarily, moving away from the stagnation point, the temperature increases because there is a lower amount of water and the impingement water is decreasing. In this region, the surface temperature is underestimated in the results obtained with PoliMIce. This issue could be due to rivulets formation which was not modeled in this work. Indeed, the wetness fraction for rivulets is lower than one, exposing heaters surface patches to the air and this could increase the surface temperature.

From Fig. 11(b) it can be seen that the water limits are larger than the impinging ones and it means that a large amount of water does not evaporate and flows aft. However, in this test case, the runback water remains inside the protected region: the heat fluxes provided by the heater are sufficient to just evaporate the right amount of water without forming runback ice.

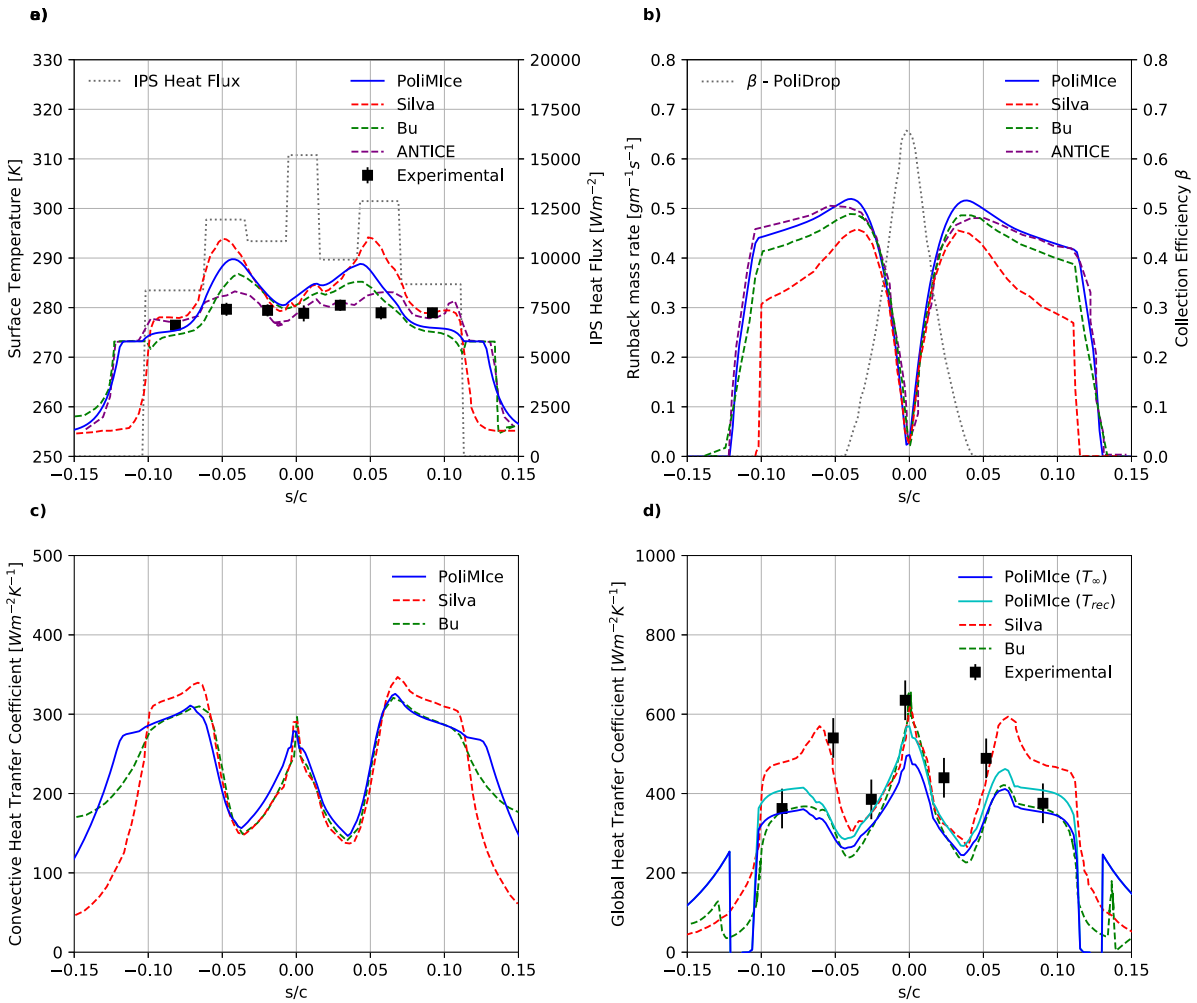

Fig. 12. Results for the testcase 67B compared with experimental results from [4] and previous simulations presented in [20,13]. In figure (a), the temperature at the surface of the airfoil is depicted. Figure (b) shows the average runback water mass flowing at the surface of the airfoil. In figure (c), the convective heat transfer coefficient obtained is presented. In figure (d) the overall heat transfer coefficient is shown.

Figs. 11(c) and 11(d) present the convective and the global heat transfer coefficients respectively, showing good agreement with reference results. It can be noticed that, as it was expected, the peak of the heat transfer coefficients is at the stagnation point and then its values decrease in the laminar region. Then it increases again during transition and decreases again in the turbulent boundary layer. There are differences in the prediction of the transition onsets and end, as discussed above.

Fig. 12 presents the results regarding test case 67B, once again showing good agreement with reference results. As expected, the surface temperature shown in Fig. 12(a) is lower with respect to test case 67A. The environment and flight conditions are the same for both test cases but the heat fluxes set in 67B are lower: this causes reduced evaporation and therefore, a larger amount of water is liquid and runs downstream. It can be noticed in Fig. 12(b) that the runback mass of water reaches the end of the protected region leading to the formation of runback ice. This is clear by the trend of the surface temperature: at the limits of the heaters, there is a region where the temperature remains constant and equal to the freezing temperature. This behavior is due to the release of the freezing latent heat during phase change. This trend is also observed for ANTICE and Bu models, but not for Silva model as they did not include a freezing model. The differences in the temperature profile arise from the prediction of the heat transfer coefficient, which affects both evaporative and convective fluxes. In this, Silva et al. and Bu et al. works, the boundary layer model is the same. However, as for the transition model, there might be differences on the numerical schemes, the selection of the temperature to assess the air properties and the definition of the model itself.

Figs. 12(c) and 12(d) show the convective and global heat transfer coefficients. It can be noticed that there is a discontinuity at the end of the runback water, caused by the way the global heat transfer coefficient is defined: where no water is present, the heat transfer coefficient is set equal to h_{air}, causing the discontinuity. Moreover, that is the region

where ice formation occurs, therefore the heat is then released resulting in negative heat fluxes. The results for test case 67B show that the power supplied by the heaters is not enough to prevent ice formation in these conditions. The water is not evaporated within the protected region, leading to runback ice formation. This is a very dangerous situation for the airworthiness of the aircraft, because the ice cannot be removed by the IPS leading to aerodynamic performance degradation and to possible serious accidents. Besides, it can be seen there are larger differences in U computed with T_{rec} and T_∞ than those observed in Figs. 10(d) and 11(d), for which both plots nearly overlap. When the values of T_{wall} are lower, such as in the case 67B, the difference between T_{rec} and T_∞ become proportionally more evident in ΔT and in the calculations of U. Better results are obtained when computing U with T_{rec}, as in the reference calculations. However, the profile of T_{rec} is unavailable experimentally. Therefore, the deviations in the U with respect to the experimental measurements may present larger deviations than those reported in the literature.

6. Conclusions

In this work, a model for a 2D electro-thermal Ice Protection System has been developed and implemented in the PoliMIce framework. Given the results from flowfield and particle tracking computations, the model provides results regarding surface temperature, runback mass of water and heat transfer coefficients.

The model and the numerical code have been validated against experimental data and numerical simulations from open literature. The results obtained with PoliMIce were in good agreement with reference data. Particularly the transition model allowed to obtain an accurate computation of the heat transfer coefficient.

One drawback of the present model is that it includes a transition model based on empirical observations, similarly to other models available in the open literature. The empirical correlation was formulated based on a reduced set of experiments. In this case, the predictions were appropriate but the same may not happen for different angles of attack or higher Reynolds numbers. Moreover, the transition model relies on an input parameter (turbulence intensity), which in this case has been taken from reference literature. In case there are no experimental data this parameter must be assumed. Therefore, there is the need of a model with no input parameters for a more robust simulation.

The computation of the runback water mass with the proposed liquid film model led to similar mass rate predictions than those obtained by Bu et al. [13] and with ANTICE [4]. In test case 67B the present IPS model was able to predict the runback ice formation. The largest discrepancy was found in the solid surface temperature at the limits of the runback water. This could be due to rivulets formation, whose modelling is not yet included. Moreover, the local temperature profile across the height the liquid film should be taken into account to get a more accurate description of the phenomenon as well as more sophisticated conduction models in the solid substratum. Lastly, the presented model is applicable only to a 2D simulation.

As a conclusion, it can be stated that the present code is capable to accurately predict the performance of an anti-ice electro-thermal system in both evaporative and running-wet regimes. This code can be therefore used as an efficient tool in the design process of an ice protection system.

Acknowledgment

The work in this paper was supported in part by the H2020-MSCA-ITN-2016 UTOPIAE, grant agreement 722734.

References

[1] R. Gent, N. Dart, J. Cansdale, Aircraft icing, Phil. Trans. R. Soc. A 358 (1776) (2000) 2873–2911.
[2] J. Steuernagle, K. Roy, David, Aircraft Icing, Tech. Rep., 2008.
[3] D. Lou, D.W. Hammond, Heat and mass transfer for ice particle ingestion inside aero-engine, J. Turbomach. 133 (3) (2011).
[4] K.M. Al-Khalil, C. Horvath, D.R. Miller, W.B. Wright, Validation of NASA Thermal Ice Protection Computer Codes. Part 3; The Validation of Antice, 2001.
[5] S. Kutluay, A. Bahadir, A. Özdeş, The numerical solution of one-phase classical Stefan problem, J. Comput. Appl. Math. 81 (1) (1997) 135–144.
[6] N. Calvo, J. Durany, C. Vázquez, Finite elements numerical solution of a coupled profile–velocity–temperature shallow ice sheet approximation model, J. Comput. Appl. Math. 158 (1) (2003) 31–41.
[7] S. Stepanov, M. Vasilyeva, V.I. Vasil'ev, Generalized multiscale discontinuous Galerkin method for solving the heat problem with phase change, J. Comput. Appl. Math. 340 (2018) 645–652.
[8] K. Al-Khalil, T. Keith, J. De Witt, Development of an anti-icing runback model, in: 28th Aerospace Sciences Meeting, 1990, pp. 759.
[9] K. Al-Khalil, T. Keith, J. De Witt, Further development of an anti-icing runback model, in: 29th Aerospace Sciences Meeting, 1991, pp. 266.
[10] G.A. Ruff, B.M. Berkowitz, Users Manual for the NASA Lewis Ice Accretion Prediction Code (LEWICE), 1990.
[11] F. Morency, F. Tezok, I. Paraschivoiu, Anti-icing system simulation using CANICE, J. Aircr. 36 (6) (1999) 999–1006.
[12] G. Silva, O. Silvares, E. Zerbini, Airfoil anti-ice system modeling and simulation, in: 41st Aerospace Sciences Meeting and Exhibit, American Institute of Aeronautics and Astronautics, 2003.
[13] X. Bu, G. Lin, J. Yu, S. Yang, X. Song, Numerical simulation of an airfoil electrothermal anti-icing system, Proc. Inst. Mech. Eng. G 227 (10) (2013) 1608–1622.
[14] W.M. Kays, Convective Heat and Mass Transfer, Tata McGraw-Hill Education, 2012.
[15] T. Cebeci, P. Bradshaw, Physical and Computational Aspects of Convective Heat Transfer, Springer Science & Business Media, 2012.
[16] G. Ambrok, Approximate solution of equations for the thermal boundary layer with variations in boundary layer structure, Sov. Phys.-Tech. Phys. 2 (9) (1957) 1979–1986.
[17] F. Morency, F. Tezok, I. Paraschivoiu, Heat and mass transfer in the case of anti-icing system simulation, J. Aircr. 37 (2) (2000) 245–252.

[18] G.A.L. da Silva, O. de Mattos Silvares, E.J.G. de Jesus Zerbini, Numerical simulation of airfoil thermal anti-ice operation, part 1: Mathematical modelling, J. Aircr. 44 (2) (2007) 627–633.
[19] B.L. Messinger, Equilibrium temperature of an unheated icing surface as a function of air speed, J. Aeronaut. Sci. 20 (1) (1953) 29–42.
[20] G.A.L. da Silva, O. de Mattos Silvares, E.J.G. de Jesus Zerbini, H. Hefazi, H.-H. Chen, K. Kaups, Differential boundary-layer analysis and runback water flow model applied to flow around airfoils with thermal anti-ice, in: 1st AIAA Atmospheric and Space Environments Conference, 2009, pp. 3967.
[21] T. Myers, J. Charpin, S. Chapman, Modelling the flow and solidification of a thin liquid film on a three-dimensional surface, in: Progress in Industrial Mathematics At ECMI 2004, Springer, 2006, pp. 508–512.
[22] G. Gori, M. Zocca, M. Garabelli, A. Guardone, G. Quaranta, PoliMIce: A simulation framework for three-dimensional ice accretion, Appl. Math. Comput. 267 (2015) 96–107.
[23] M. Zocca, G. Gori, A. Guardone, Blockage and three-dimensional effects in wind-tunnel testing of ice accretion over wings, J. Aircraft 54 (2) (2016) 759–767.
[24] G. Gori, G. Parma, M. Zocca, A. Guardone, Local solution to the unsteady stefan problem for in-flight ice accretion modeling, J. Aircraft 55 (1) (2017) 251–262.
[25] F. Palacios, J. Alonso, K. Duraisamy, M. Colonno, J. Hicken, A. Aranake, A. Campos, S. Copeland, T. Economon, A. Lonkar, et al., Stanford University unstructured, SU2: An open-source integrated computational environment for multi-physics simulation and design, in: 51st AIAA Aerospace Sciences Meeting Including the New Horizons Forum and Aerospace Exposition, 2013, pp. 287.
[26] T. Bellosta, G. Parma, A. Guardone, A Robust 3D particle tracking solver of in-flight ice accretion using, arbitrary precision arithmetics, in: VIII International Conference on Coupled Problems in Science and Engineering, 2019.
[27] G.A.L. da Silva, O. de Mattos Silvares, E.J.G. de Jesus Zerbini, Numerical simulation of airfoil thermal anti-ice operation, part 2: Implementation and results, J. Aircr. 44 (2) (2007) 634–641.
[28] B. Abu-Ghannam, R. Shaw, Natural transition of boundary layers—the effects of turbulence, pressure gradient, and flow history, J. Mech. Eng. Sci. 22 (5) (1980) 213–228.
[29] H. Beaugendre, F. Morency, W. Habashi, Development of a second generation in-flight icing simulation code, J. Fluids Eng. 128 (2006) 378–387.
[30] R. Chauvin, L. Bennani, P. Trontin, P. Villedieu, An implicit time marching Galerkin method for the simulation of icing phenomena with a triple layer model, Finite Elem. Anal. Des. 150 (2018) 20–33.
[31] J.A. Goff, Low-pressure properties of water-from 160 to 212 F, Trans. Am. Soc. Heat. Vent. Eng. 52 (1946) 95–121.
[32] W. Wright, K. Dewitt, J. Keith, Numerical simulation of icing, deicing, and shedding, in: 29th Aerospace Sciences Meeting, 1991, pp. 665.
[33] T. Reid, G.S. Baruzzi, W.G. Habashi, FENSAP-ICE: Unsteady conjugate heat transfer simulation of electrothermal de-icing, J. Aircr. 49 (4) (2012) 1101–1109.
[34] D. Miller, T. Bond, D. Sheldon, W. Wright, T. Langhals, K. Al-Khalil, H. Broughton, Validation of NASA thermal ice protection computer codes. Part 1; Program overview, in: AIAA 35th Aerospace Sciences Meeting, Reno, NV, pp. 97–0049, 1997.
[35] P.L. Roe, Approximate Riemann solvers, parameter vectors, and difference schemes, J. Comput. Phys. 43 (2) (1981) 357–372.